A conservative numerical method for the Cahn–Hilliard equation in complex domains

Jaemin Shin, Darae Jeong, Junseok Kim *

Department of Mathematics, Korea University, Seoul 136-701, Republic of Korea

ARTICLE INFO

ABSTRACT

We propose an efficient finite difference scheme for solving the Cahn–Hilliard equation with a variable mobility in complex domains. Our method employs a type of unconditionally gradient stable splitting discretization. We also extend the scheme to compute the Cahn–Hilliard equation in arbitrarily shaped domains. We prove the mass conservation property of the proposed discrete scheme for complex domains. The resulting discretized equations are solved using a multigrid method. Numerical simulations are presented to demonstrate that the proposed scheme can deal with complex geometries robustly. Furthermore, the multigrid efficiency is retained even if the embedded domain is present.

© 2011 Elsevier Inc. All rights reserved.

1. Introduction

In this paper, we consider an efficient finite difference scheme for the Cahn–Hilliard (CH) equation with a variable mobility in complex domains.

$$\frac{\partial \phi(\mathbf{x}, t)}{\partial t} = \nabla \cdot [M(\phi(\mathbf{x}, t)) \nabla \mu(\phi(\mathbf{x}, t))], \quad \mathbf{x} \in \Omega, \quad 0 < t \leqslant T, \tag{1}$$

$$\mu(\phi(\mathbf{x}, t)) = F'(\phi(\mathbf{x}, t)) - \epsilon^2 \Delta \phi(\mathbf{x}, t), \tag{2}$$

where $\Omega \subset \mathbb{R}^d (d = 1, 2, 3)$ is a domain, $\phi = m_A - m_B$ is a difference of molar fractions m_A and m_B of species A and B, and $M(\phi)$ is a nonnegative diffusional mobility. $F(\phi)$ is the free energy density of a homogeneous fluid and ϵ is a positive constant. The CH equation has the total free energy functional:

$$\mathscr{E}(\phi) = \int_\Omega \left(F(\phi) + \frac{\epsilon^2}{2} |\nabla \phi|^2 \right) d\mathbf{x}. \tag{3}$$

The CH equation was originally introduced to describe the complicated phase separation and coarsening phenomena called the spinodal decomposition in binary alloys [5,6]. We also define the quantity c as the molar fraction m_A, i.e., $c = m_A$. Note that $\phi = 2c - 1$. Typical forms of the free energy are given as [11]

$$F(\phi) = \frac{(1 - \phi^2)^2}{4} \quad \text{and} \quad F(c) = \frac{c^2(1 - c)^2}{4}. \tag{4}$$

* Corresponding author. Tel.: +82 2 3290 3077; fax: +82 2 929 8562.
E-mail addresses: cfdkim@korea.ac.kr, cfdkim@dongguk.edu (J. Kim).
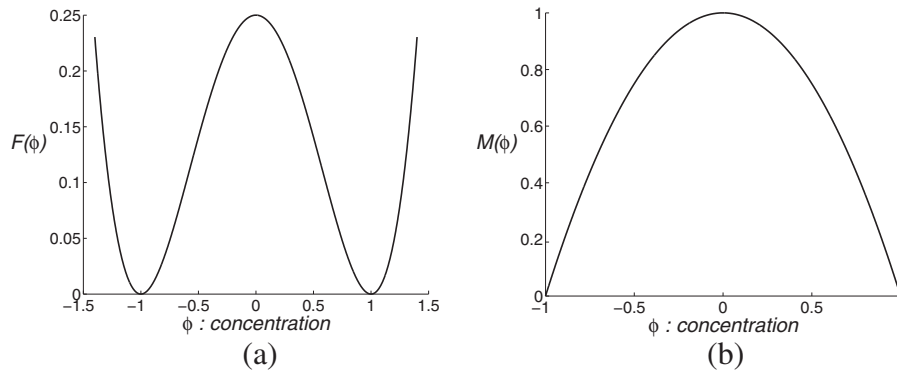URL: http://math.korea.ac.kr/~cfdkim/ (J. Kim).

Fig. 1. (a) Free energy $F(\phi)$. (b) Variable diffusional mobility $M(\phi)$.

The free energy has a double-well potential that has local minima at the minimum and maximum of the concentration as shown in Fig. 1(a). And we take variable mobilities of the form

$$M(\phi) = 1 - \phi^2 \quad \text{and} \quad M(c) = c(1 - c) \tag{5}$$

which are degenerated at the minimum and maximum of the concentration as shown in Fig. 1(b) [7]. This mobility significantly lowers the long-range diffusion across bulk regions with the enhanced diffusion in the interfacial region. The system is completed by taking an initial condition and the natural and no-flux boundary conditions $\mathbf{n} \cdot \nabla \phi = \mathbf{n} \cdot \nabla \mu = 0$ on $\partial \Omega$, where $\mathbf{n}$ is a unit normal vector to $\partial \Omega$.

In the original derivation of the CH equation, a concentration dependent mobility appeared [4–6]. Various numerical methods have been applied to solve the CH equation with a constant mobility [1,9,12,14,15,17,22,25,27,32]. However, relatively few authors have considered the CH equation with a concentration dependent mobility [2,3,16,19–21,26,30,31,33].

In this paper, we propose an efficient finite difference scheme for the CH equation with a variable mobility. Furthermore, we also extend the scheme to compute the CH equation in arbitrarily shaped domains. The application of Cartesian mesh for solving problems with complex geometry has been used in the past decade. Many authors have studied the Cartesian grid method and the finite volume method for solving the Poisson equation with an irregular domain [8,10,18,23,29]. Cartesian grid embedded boundary methods have advantages over unstructured grid methods because of simpler grid generation.

This paper is organized as follows. In Section 2, we describe the numerical solution of the CH equation with a variable mobility and the details of the treatment of arbitrarily shaped domains. The numerical results showing the robustness and superiority of the proposed scheme with a variable mobility are described in Section 3. Conclusions are presented in Section 4.

2. Numerical methods

2.1. Numerical discretization

2.1.1. The Cahn–Hilliard equation in a rectangular domain

In this section, we present fully discrete schemes for the CH equation in a rectangular domain. For simplicity of exposition, we shall discretize the CH Eqs. (1) and (2) in two-dimensional space $\Omega = (a, b) \times (c, d)$. Three-dimensional discretization is analogously defined. Let N_x and N_y be positive even integers, $\Delta x = (b - a)/N_x$ and $\Delta y = (d - c)/N_y$ be the uniform mesh sizes. We assume $h = \Delta x = \Delta y$. Also let $\Omega^h = \{(x_i, y_j): x_i = a + (i - 0.5)h, y_j = c + (j - 0.5)h, 1 \leqslant i \leqslant N_x, 1 \leqslant j \leqslant N_y\}$ be the set of cell-centers. Let ϕ_{ij}^n and μ_{ij}^n be approximations of $\phi(x_i, y_j, t_n)$ and $\mu(x_i, y_j, t_n)$, where $t_n = n \Delta t$ and Δt is the time step. We use zero Neumann boundary condition for ϕ and μ at the domain boundary, for example

$$D_x \phi_{\frac{1}{2}j} = D_x \phi_{N_x + \frac{1}{2}j} = D_y \phi_{i,\frac{1}{2}} = D_y \phi_{i,N_y + \frac{1}{2}} = 0,$$

where the discrete differentiation operators are

$$D_x \phi_{i+\frac{1}{2}j} = \frac{\phi_{i+1j} - \phi_{ij}}{h} \quad \text{and} \quad D_y \phi_{i,j+\frac{1}{2}} = \frac{\phi_{i,j+1} - \phi_{ij}}{h}.$$

And we use the notation $\nabla_d \phi_{ij} = \left(D_x \phi_{i+\frac{1}{2}j}, D_y \phi_{i,j+\frac{1}{2}} \right)$ to represent the discrete gradient of ϕ at cell-edges. Correspondingly, the divergence at cell-centers, using values from cell-edges, is $\nabla_d \cdot \left(D_x \phi_{i+\frac{1}{2}j}, D_y \phi_{i,j+\frac{1}{2}} \right)_{ij} = \left(D_x \phi_{i+\frac{1}{2}j} - D_x \phi_{i-\frac{1}{2}j} + D_y \phi_{i,j+\frac{1}{2}} - D_y \phi_{i,j-\frac{1}{2}} \right)/h$. Then we define the discrete Laplacian by $\Delta_d \phi_{ij} := \nabla_d \cdot \nabla_d \phi_{ij}$ and the discrete l_2 inner products by

$$(c,d)_h := h^2 \sum_{i=1}^{N_x} \sum_{j=1}^{N_y} c_{ij} d_{ij},$$

$$(\nabla_d c, \nabla_d d)_e := h^2 \left(\sum_{i=0}^{N_x} \sum_{j=1}^{N_y} D_x c_{i+\frac{1}{2}j} D_x d_{i+\frac{1}{2}j} + \sum_{i=1}^{N_x} \sum_{j=0}^{N_y} D_y c_{i,j+\frac{1}{2}} D_y d_{i,j+\frac{1}{2}} \right).$$

We also define discrete norms as $|c|_2^2 = (c,c)_h$ and $|c|_1^2 = (\nabla_d c, \nabla_d c)_e$.

In Ref. [20], a Crank–Nicolson (CN) method for the CH equation was proposed as follows:

$$\frac{c_{ij}^{n+1} - c_{ij}^n}{\Delta t} = \nabla_d \cdot \left(M(c)_{ij}^{n+\frac{1}{2}} \nabla_d \mu_{ij}^{n+\frac{1}{2}} \right), \tag{6}$$

$$\mu_{ij}^{n+\frac{1}{2}} = \frac{1}{2} \left(F'(c_{ij}^{n+1}) + F'(c_{ij}^n) \right) - \frac{\epsilon^2}{2} \Delta_d (c_{ij}^{n+1} + c_{ij}^n), \tag{7}$$

where $M(c)_{i+\frac{1}{2}j}^{n+\frac{1}{2}} := M\left((c_{ij}^n + c_{i+1j}^n + c_{ij}^{n+1} + c_{i+1j}^{n+1})/4 \right)$. This CN method has second-order accuracy in time and space. However, it has a severe time step restriction.

In this paper, we present a semi-implicit time and centered difference space discretization of Eqs. (1) and (2). For the phase-field variable c, we have the following discretization:

$$\frac{c_{ij}^{n+1} - c_{ij}^n}{\Delta t} = \nabla_d \cdot \left(M(c)_{ij}^n \nabla_d \mu_{ij}^{n+\frac{1}{2}} \right), \tag{8}$$

$$\mu_{ij}^{n+\frac{1}{2}} = \frac{1}{2} c_{ij}^{n+1} - \epsilon^2 \Delta_d c_{ij}^{n+1} + F'(c_{ij}^n) - \frac{1}{2} c_{ij}^n \tag{9}$$

and for the phase-field variable ϕ, we have the following one:

$$\frac{\phi_{ij}^{n+1} - \phi_{ij}^n}{\Delta t} = \nabla_d \cdot \left(M(\phi)_{ij}^n \nabla_d \mu_{ij}^{n+\frac{1}{2}} \right), \tag{10}$$

$$\mu_{ij}^{n+\frac{1}{2}} = 2\phi_{ij}^{n+1} - \epsilon^2 \Delta_d \phi_{ij}^{n+1} + F'(\phi_{ij}^n) - 2\phi_{ij}^n, \tag{11}$$

where

$$\nabla_d \cdot \left(M(\phi)_{ij}^n \nabla_d \mu_{ij}^{n+\frac{1}{2}} \right) := \frac{M_{i+\frac{1}{2}j}^n \left(\mu_{i+1j}^{n+\frac{1}{2}} - \mu_{ij}^{n+\frac{1}{2}} \right) - M_{i-\frac{1}{2}j}^n \left(\mu_{ij}^{n+\frac{1}{2}} - \mu_{i-1j}^{n+\frac{1}{2}} \right)}{h^2} + \frac{M_{i,j+\frac{1}{2}}^n \left(\mu_{i,j+1}^{n+\frac{1}{2}} - \mu_{ij}^{n+\frac{1}{2}} \right) - M_{i,j-\frac{1}{2}}^n \left(\mu_{ij}^{n+\frac{1}{2}} - \mu_{i,j-1}^{n+\frac{1}{2}} \right)}{h^2}. \tag{12}$$

Here $M_{i+\frac{1}{2}j}^n = M\left((\phi_{i+1j}^n + \phi_{ij}^n)/2 \right)$ and the other terms are similarly defined. We note that if the mobility $M(\phi)$ is constant, then the discrete schemes (8)–(11) become unconditionally gradient stable linear splitting schemes [13].

During computation, the values of the concentration c can be negative or greater than one and also ϕ has a similar case. For physical relevance of the solution, we want the non-negative mobility ($M(\cdot) \geq 0$), therefore we use $M(c) = |c(1-c)|$ and $M(\phi) = |1 - \phi^2|$ for numerical evaluations with the concentration dependent mobility.
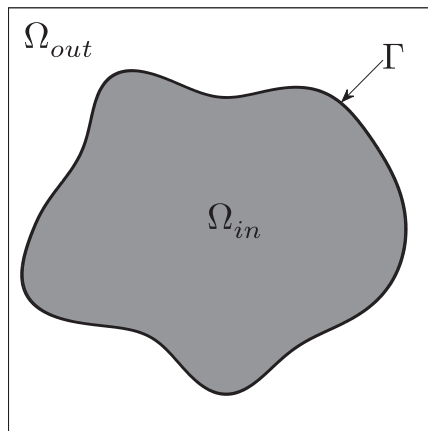

Fig. 2. Shaded area Ω_{in} is embedded in Ω and Ω_{out} is defined as $\Omega \setminus \Omega_{in} = \Omega \cap \Omega_{in}^c$.

2.1.2. The Cahn–Hilliard equation in a non-rectangular domain

Now, we give a numerical scheme for the CH equation in a non-rectangular domain with homogeneous Neumann boundary conditions. Let Ω_{in} be an arbitrarily shaped open domain which is embedded in Ω. Also, let $\Gamma = \partial \Omega_{in}$ be the arbitrarily shaped domain boundary (see Fig. 2).

To solve Eqs. (10) and (11) in an arbitrarily shaped domain Ω_{in}, we propose the following numerical scheme:

$$\frac{\phi_{ij}^{n+1} - \phi_{ij}^n}{\Delta t} = \nabla_d \cdot \left(G_{ij} M(\phi_{ij}^n) \nabla_d \mu_{ij}^{n+\frac{1}{2}} \right), \tag{13}$$

$$\mu_{ij}^{n+\frac{1}{2}} = 2\phi_{ij}^{n+1} - \epsilon^2 \nabla_d \cdot \left(G_{ij} \nabla_d \phi_{ij}^{n+1} \right) + F'(\phi_{ij}^n) - 2\phi_{ij}^n. \tag{14}$$

Here the boundary control function G is defined in Ω^h by

$$G(x,y) = \begin{cases} 1 & \text{if } (x,y) \in \Omega_{in}^h, \\ 0 & \text{if } (x,y) \in \Omega_{out}^h = \Omega \setminus \Omega_{in}^h, \end{cases} \tag{15}$$

where Ω_{in}^h is an open region that consists of interior points of the union of the closed cells whose centers are inside the interface Γ. For example, in Fig. 3 the value of function G at points $(\times, \circ)$ in Ω_{out}^h is zero. The value of function G at point $(\bullet, \circ)$ in Ω_{in}^h is one.

As we refine the mesh, i.e., $h \to 0$, the arbitrarily shaped domain Ω_{in} is approximated by Ω_{in}^h (see Fig. 4).

2.2. Conservation property of the total mass

In this section, we show that our scheme inherits the conservation of total mass in a complex domain. We want to show that

$$\sum\nolimits_{ij \in \Omega_{in}} \phi_{ij}^{n+1} = \sum\nolimits_{ij \in \Omega_{in}} \phi_{ij}^n \quad \text{for all } n = 0, 1, \ldots. \tag{16}$$

We start by summing Eq. (13) in the whole numerical domain Ω, i.e.,

$$\sum\nolimits_{ij \in \Omega} \frac{\phi_{ij}^{n+1} - \phi_{ij}^n}{\Delta t} = \frac{1}{h^2} \sum\nolimits_{ij \in \Omega} \left[G_{i+\frac{1}{2}j} M_{i+\frac{1}{2}j}^n \left(\mu_{i+1,j}^{n+\frac{1}{2}} - \mu_{ij}^{n+\frac{1}{2}} \right) - G_{i-\frac{1}{2}j} M_{i-\frac{1}{2}j}^n \left(\mu_{ij}^{n+\frac{1}{2}} - \mu_{i-1,j}^{n+\frac{1}{2}} \right) \right.$$
$$\left. + G_{ij+\frac{1}{2}} M_{ij+\frac{1}{2}}^n \left(\mu_{ij+1}^{n+\frac{1}{2}} - \mu_{ij}^{n+\frac{1}{2}} \right) - G_{ij-\frac{1}{2}} M_{ij-\frac{1}{2}}^n \left(\mu_{ij}^{n+\frac{1}{2}} - \mu_{ij-1}^{n+\frac{1}{2}} \right) \right]$$
$$= \frac{1}{h^2} \sum\nolimits_{j=1}^{N_y} \left[G_{N_x+\frac{1}{2}j} M_{N_x+\frac{1}{2}j}^n \left(\mu_{N_x+1,j}^{n+\frac{1}{2}} - \mu_{N_x j}^{n+\frac{1}{2}} \right) - G_{\frac{1}{2}j} M_{\frac{1}{2}j}^n \left(\mu_{1j}^{n+\frac{1}{2}} - \mu_{0j}^{n+\frac{1}{2}} \right) \right]$$
$$+ \frac{1}{h^2} \sum\nolimits_{i=1}^{N_x} \left[G_{i,N_y+\frac{1}{2}} M_{i,N_y+\frac{1}{2}}^n \left(\mu_{i,N_y+1}^{n+\frac{1}{2}} - \mu_{i,N_y}^{n+\frac{1}{2}} \right) - G_{i,\frac{1}{2}} M_{i,\frac{1}{2}}^n \left(\mu_{i1}^{n+\frac{1}{2}} - \mu_{i0}^{n+\frac{1}{2}} \right) \right]. \tag{17}$$

Then, by applying zero Neumann boundary condition of $\mu_{ij}^{n+\frac{1}{2}}$ on $\partial \Omega$, we obtain

$$\sum\nolimits_{ij \in \Omega} \frac{\phi_{ij}^{n+1} - \phi_{ij}^n}{\Delta t} = 0, \quad \text{i.e.,} \quad \sum\nolimits_{ij \in \Omega} \phi_{ij}^{n+1} = \sum\nolimits_{ij \in \Omega} \phi_{ij}^n. \tag{18}$$
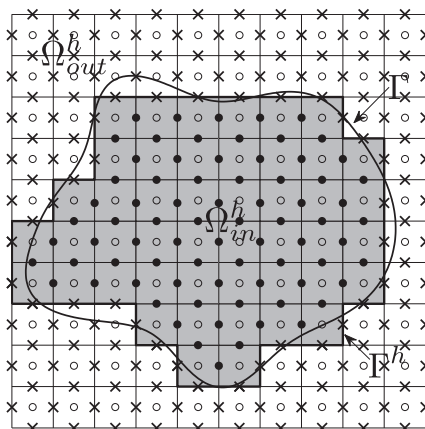

Fig. 3. Shaded area Ω_{in}^h is embedded in Ω and Ω_{out}^h is defined as $\Omega \cap \Omega_{in}^{h^c}$. Note that the value of function G at points $(\times, \circ)$ in Ω_{out}^h is zero.
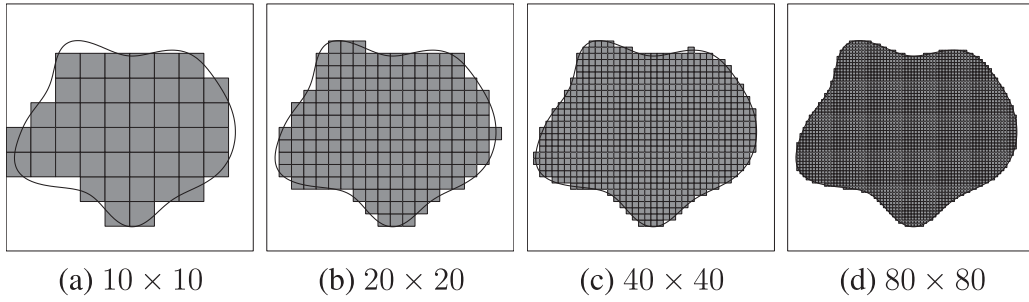
(a) 10×10 (b) 20×20 (c) 40×40 (d) 80×80

Fig. 4. Convergence of Ω_{in}^h to Ω_{in} as we refine the mesh. Mesh sizes are shown below each figure.

Next, we consider summation of Eq. (13) in the outside numerical domain Ω_{out}, i.e.,

$$\sum_{ij \in \Omega_{out}} \frac{\phi_{ij}^{n+1} - \phi_{ij}^n}{\Delta t} = \frac{1}{h^2} \sum_{ij \in \Omega_{out}} \left[G_{i+\frac{1}{2}j} M_{i+\frac{1}{2}j}^n \left(\mu_{i+1j}^{n+\frac{1}{2}} - \mu_{ij}^{n+\frac{1}{2}} \right) - G_{i-\frac{1}{2}j} M_{i-\frac{1}{2}j}^n \left(\mu_{ij}^{n+\frac{1}{2}} - \mu_{i-1j}^{n+\frac{1}{2}} \right) + G_{ij+\frac{1}{2}} M_{ij+\frac{1}{2}}^n \left(\mu_{ij+1}^{n+\frac{1}{2}} - \mu_{ij}^{n+\frac{1}{2}} \right) \right.$$
$$\left. - G_{ij-\frac{1}{2}} M_{ij-\frac{1}{2}}^n \left(\mu_{ij}^{n+\frac{1}{2}} - \mu_{ij-1}^{n+\frac{1}{2}} \right) \right] = 0, \tag{19}$$

where we have used the assumption (15) that G is zero in Ω_{out}. By using the above property (18), we obtain

$$\sum_{ij \in \Omega_{in}} \phi_{ij}^{n+1} = \sum_{ij \in \Omega} \phi_{ij}^n - \sum_{ij \in \Omega_{out}} \phi_{ij}^{n+1} = \sum_{ij \in \Omega_{in}} \phi_{ij}^n + \sum_{ij \in \Omega_{out}} \phi_{ij}^n - \sum_{ij \in \Omega_{out}} \phi_{ij}^{n+1} = \sum_{ij \in \Omega_{in}} \phi_{ij}^n - \Delta t \sum_{ij \in \Omega_{out}} \frac{\phi_{ij}^{n+1} - \phi_{ij}^n}{\Delta t}$$
$$= \sum_{ij \in \Omega_{in}} \phi_{ij}^n,$$

where we have used Eq. (19) in the last equality. Therefore, we proved the conservation property of mass, Eq. (16), in a complex domain Ω_{in}.

2.3. Numerical algorithm

In this section, we show the way to control a matrix in finer and coarser grids with the boundary control function G. And we describe the multigrid method and implementation in detail to solve the resulting coupled system of equations.

First we set the boundary control matrix function G as defined in Eq. (15) to represent a complex domain. In Figs. 3 and 5, the cell-edge ($\bullet, \times$) values are used in the smoothing step and the cell-center ($\circ$) values are used in the restriction and interpolation operators. Denote that G^h is a discrete boundary control function defined in Ω^h. In the coarser grid Ω^H, the control function G^H is different from G^h because Ω^H is defined as shown in Fig. 5. The details about the coarser domain Ω^H are explained by the restriction and interpolation operators. Note that as a set we have the following inclusion: $\Omega_{in}^h \subset \Omega_{in}^H$.

Next, we describe a full approximation storage (FAS) multigrid method to solve the discrete system (13) and (14) at the implicit time level. A pointwise Gauss–Seidel relaxation is used as the smoother in the multigrid method. See the reference text [28] for additional details and backgrounds. The algorithm of the multigrid method for solving the discrete CH system is: First, let us rewrite Eqs. (13) and (14) as follows.
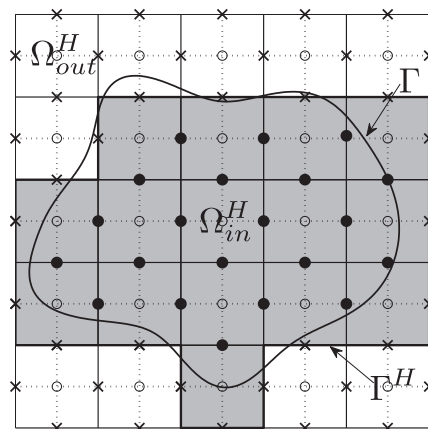

Fig. 5. Illustration of the coarsening process for the multigrid method. Shaded area Ω_{in}^H is also embedded in Ω but is not generally same to Ω_{in}^h, i.e., $\Omega_{in}^h \subset \Omega_{in}^H$.

$$L(\phi^{n+1},\mu^{n+\frac{1}{2}})=(\xi^n,\psi^n), \quad \text{where } L(\phi^{n+1},\mu^{n+\frac{1}{2}})$$
$$=\left(\phi_{ij}^{n+1}/\Delta t-\nabla_d\cdot\left(G_{ij}M(\phi_{ij}^n)\nabla_d\mu_{ij}^{n+\frac{1}{2}}\right),\ \epsilon^2\nabla_d\cdot\left(G_{ij}\nabla_d\phi_{ij}^{n+1}\right)-2\phi_{ij}^{n+1}+\mu_{ij}^{n+\frac{1}{2}}\right)$$

and the source term is $(\xi^n,\psi^n)=\left(\phi_{ij}^n/\Delta t,F'(\phi_{ij}^n)-2\phi_{ij}^n\right)$.

In the following description of one FAS cycle, Ω^H is coarser than Ω^h by factor 2. Given the number v_1 and v_2 of pre-and post-smoothing relaxation sweeps, an iteration step for the multigrid method using the V-cycle is formally written as in Fig. 6 [28]. In Fig. 6, $\{\phi^{n+1,m},\mu^{n+\frac{1}{2},m}\}$ and $\{\hat{\phi}^{n+1,m+1},\hat{\mu}^{n+\frac{1}{2},m+1}\}$ are the approximations of $\phi^{n+1}(x_i,y_j)$ and $\mu^{n+\frac{1}{2}}(x_i,y_j)$ before and after an FAS cycle.

The FAS multigrid algorithm in Fig. 6 consists of the following components.

- Smoothing:

$$\{\bar{\phi}^{n+1,m},\bar{\mu}^{n+\frac{1}{2},m}\}=SMOOTH^{v_1}(\phi^{n+1,m},\mu^{n+\frac{1}{2},m},L_h,\xi^n,\psi^n),$$

which means performing v_1-smoothing steps with the initial approximations $\phi^{n+1,m},\mu^{n+\frac{1}{2},m}$, source terms ξ^n,ψ^n, and *SMOOTH* relaxation operator to get the approximations $\bar{\phi}^{n+1,m}$ and $\bar{\mu}^{n+\frac{1}{2},m}$. One *SMOOTH* relaxation operator step consists of solving the system (22) and (23) given below by 2×2 matrix inversion for each i and j. Here, we derive the smoothing operator in two dimensions. Rewriting Eq. (13), we get

$$\frac{\phi_{ij}^{n+1,m}}{\Delta t}+\frac{G_{i+\frac{1}{2}j}M_{i+\frac{1}{2}j}^n+G_{i-\frac{1}{2}j}M_{i-\frac{1}{2}j}^n+G_{ij+\frac{1}{2}}M_{ij+\frac{1}{2}}^n+G_{ij-\frac{1}{2}}M_{ij-\frac{1}{2}}^n}{h^2}\mu_{ij}^{n+\frac{1}{2},m}$$
$$=\xi_{ij}^n+\frac{G_{i+\frac{1}{2}j}M_{i+\frac{1}{2}j}^n\mu_{i+1j}^{n+\frac{1}{2},m}+G_{i-\frac{1}{2}j}M_{i-\frac{1}{2}j}^n\mu_{i-1j}^{n+\frac{1}{2},m}}{h^2}+\frac{G_{ij+\frac{1}{2}}M_{ij+\frac{1}{2}}^n\mu_{ij+1}^{n+\frac{1}{2},m}+G_{ij-\frac{1}{2}}M_{ij-\frac{1}{2}}^n\mu_{ij-1}^{n+\frac{1}{2},m}}{h^2}. \tag{20}$$

Also, by rewriting Eq. (14), we obtain

$$-\left[\frac{\epsilon^2}{h^2}\left(G_{i+\frac{1}{2}j}+G_{i-\frac{1}{2}j}+G_{ij+\frac{1}{2}}+G_{ij-\frac{1}{2}}\right)+2\right]\phi_{ij}^{n+1,m}+\mu_{ij}^{n+\frac{1}{2},m}=\psi_{ij}^n-\frac{\epsilon^2}{h^2}\left(G_{i+\frac{1}{2}j}\phi_{i+1j}^{n+1,m}+G_{i-\frac{1}{2}j}\phi_{i-1j}^{n+1,m}+G_{ij+\frac{1}{2}}\phi_{ij+1}^{n+1,m}+G_{ij-\frac{1}{2}}\phi_{ij-1}^{n+1,m}\right). \tag{21}$$
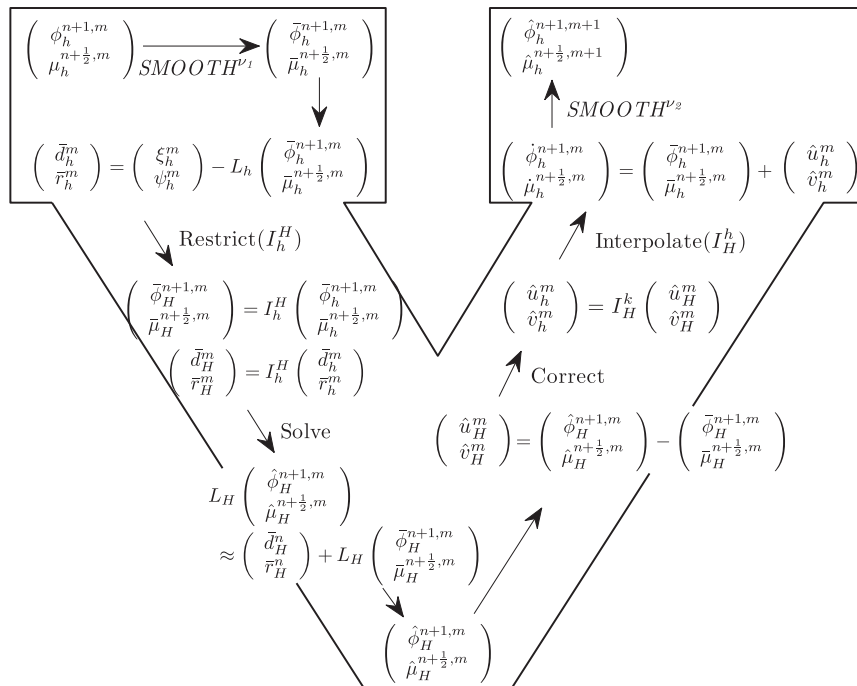
Fig. 6. The *FAS multigrid cycle* (Ω^h,Ω^H) two-grid method.

Next, we replace $\phi_{kl}^{n+1,m}$ and $\mu_{kl}^{n+\frac{1}{2},m}$ in Eqs. (20) and (21) with $\bar{\phi}_{kl}^{n+1,m}$ and $\bar{\mu}_{kl}^{n+\frac{1}{2},m}$ if $k \leqslant i$ and $l \leqslant j$, otherwise with $\phi_{kl}^{n+1,m}$ and $\mu_{kl}^{n+\frac{1}{2},m}$, i.e.,

$$
\frac{\bar{\phi}_{ij}^{n+1,m}}{\Delta t} + \frac{G_{i+\frac{1}{2}j}M_{i+\frac{1}{2}j}^n + G_{i-\frac{1}{2}j}M_{i-\frac{1}{2}j}^n + G_{ij+\frac{1}{2}}M_{ij+\frac{1}{2}}^n + G_{ij-\frac{1}{2}}M_{ij-\frac{1}{2}}^n}{h^2}\bar{\mu}_{ij}^{n+\frac{1}{2},m}
$$

$$
= \xi_{ij}^n + \frac{G_{i+\frac{1}{2}j}M_{i+\frac{1}{2}j}^n \mu_{i+1j}^{n+\frac{1}{2},m} + G_{i-\frac{1}{2}j}M_{i-\frac{1}{2}j}^n \bar{\mu}_{i-1j}^{n+\frac{1}{2},m}}{h^2} + \frac{G_{ij+\frac{1}{2}}M_{ij+\frac{1}{2}}^n \mu_{ij+1}^{n+\frac{1}{2},m} + G_{ij-\frac{1}{2}}M_{ij-\frac{1}{2}}^n \bar{\mu}_{ij-1}^{n+\frac{1}{2},m}}{h^2}. \tag{22}
$$

$$
-\left[\frac{\epsilon^2}{h^2}\left(G_{i+\frac{1}{2}j} + G_{i-\frac{1}{2}j} + G_{ij+\frac{1}{2}} + G_{ij-\frac{1}{2}}\right) + 2\right]\bar{\phi}_{ij}^{n+1,m} + \bar{\mu}_{ij}^{n+\frac{1}{2},m} = \psi_{ij}^n - \frac{\epsilon^2}{h^2}\left(G_{i+\frac{1}{2}j}\phi_{i+1j}^{n+1,m} + G_{i-\frac{1}{2}j}\bar{\phi}_{i-1j}^{n+1,m} + G_{ij+\frac{1}{2}}\phi_{ij+1}^{n+1,m} + G_{ij-\frac{1}{2}}\bar{\phi}_{ij-1}^{n+1,m}\right). \tag{23}
$$

• *Restriction*: A restriction operator I_h^H is defined as

$$
d_{ij}^H = I_h^H d_{ij}^h = \frac{1}{\Sigma_{ij}}\left(G_{2i-1,2j-1}^h d_{2i-1,2j-1}^h + G_{2i-1,2j}^h d_{2i-1,2j}^h + G_{2i,2j-1}^h d_{2i,2j-1}^h + G_{2i,2j}^h d_{2i,2j}^h\right),
$$

where $\Sigma_{ij} = G_{2i-1,2j-1}^h + G_{2i-1,2j}^h + G_{2i,2j-1}^h + G_{2i,2j}^h$ and if $\Sigma_{ij} = 0$, then we define $d_{ij}^H = 0$ (see Fig. 7(a)). For example, Fig. 7(c) shows notations and symbols on fine and coarse grids. Restriction from level-h to level-H is done as follows:

$$
d_{11}^H = \frac{1}{\Sigma_{11}}\left(G_{11}^h d_{11}^h + G_{12}^h d_{12}^h + G_{21}^h d_{21}^h + G_{22}^h d_{22}^h\right) = \frac{1}{4}\left(d_{11}^h + d_{12}^h + d_{21}^h + d_{22}^h\right),
$$

$$
d_{12}^H = 0, \quad d_{21}^H = \frac{1}{3}\left(d_{31}^h + d_{32}^h + d_{34}^h\right), \quad \text{and } d_{22}^H = \frac{1}{2}\left(d_{33}^h + d_{43}^h\right).
$$

• Interpolation: The interpolation operator I_H^h (see Fig. 7(b)) represents the prolongation of corrections from level-H to level-h and is defined as

$$
\begin{Bmatrix} d_{2i-1,2j-1}^h \\ d_{2i-1,2j}^h \\ d_{2i,2j-1}^h \\ d_{2i,2j}^h \end{Bmatrix} = I_H^h d_{ij}^H = \begin{cases} G_{2i-1,2j-1}^h d_{ij}^H & \text{for } \diamond \\ G_{2i-1,2j}^h d_{ij}^H & \text{for } * \\ G_{2i,2j-1}^h d_{ij}^H & \text{for } \triangle \\ G_{2i,2j}^h d_{ij}^H & \text{for } \circ. \end{cases} \tag{24}
$$

For example, interpolation from level-H and level-h is done as follows (see Fig. 7(c)):

$$
\begin{Bmatrix} d_{11}^h \\ d_{12}^h \\ d_{21}^h \\ d_{22}^h \end{Bmatrix} = \begin{Bmatrix} G_{11}^h d_{11}^H \\ G_{12}^h d_{11}^H \\ G_{21}^h d_{11}^H \\ G_{22}^h d_{11}^H \end{Bmatrix} = \begin{Bmatrix} d_{11}^H \\ d_{11}^H \\ d_{11}^H \\ d_{11}^H \end{Bmatrix}, \quad \begin{Bmatrix} d_{13}^h \\ d_{14}^h \\ d_{23}^h \\ d_{24}^h \end{Bmatrix} = \begin{Bmatrix} G_{13}^h d_{12}^H \\ G_{14}^h d_{12}^H \\ G_{23}^h d_{12}^H \\ G_{24}^h d_{12}^H \end{Bmatrix} = \begin{Bmatrix} 0 \\ 0 \\ 0 \\ 0 \end{Bmatrix},
$$

$$
\begin{Bmatrix} d_{31}^h \\ d_{32}^h \\ d_{41}^h \\ d_{42}^h \end{Bmatrix} = \begin{Bmatrix} G_{31}^h d_{21}^H \\ G_{32}^h d_{21}^H \\ G_{41}^h d_{21}^H \\ G_{42}^h d_{21}^H \end{Bmatrix} = \begin{Bmatrix} d_{21}^H \\ d_{21}^H \\ 0 \\ d_{21}^H \end{Bmatrix}, \quad \begin{Bmatrix} d_{33}^h \\ d_{34}^h \\ d_{43}^h \\ d_{44}^h \end{Bmatrix} = \begin{Bmatrix} G_{33}^h d_{22}^H \\ G_{34}^h d_{22}^H \\ G_{43}^h d_{22}^H \\ G_{44}^h d_{22}^H \end{Bmatrix} = \begin{Bmatrix} d_{22}^H \\ 0 \\ 0 \\ d_{22}^H \end{Bmatrix}.
$$

By the above restriction and interpolation, the proposed discretization has an effect that none of grid points in Ω_{out} participates in the evolution of values in Ω_{in}.

3. Numerical experiments

In this section, we perform the following tests: showing the relation between the ϵ value and the width of the transition layer, calculating the accuracy of the proposed method, demonstrating the multigrid efficiency, comparing stabilities of the Crank–Nicolson and the proposed scheme, investigating the effect of constant and variable mobilities in 2D and 3D, validating the total mass conservation and the total energy dissipation, and spinodal decomposition on complex domains such as a
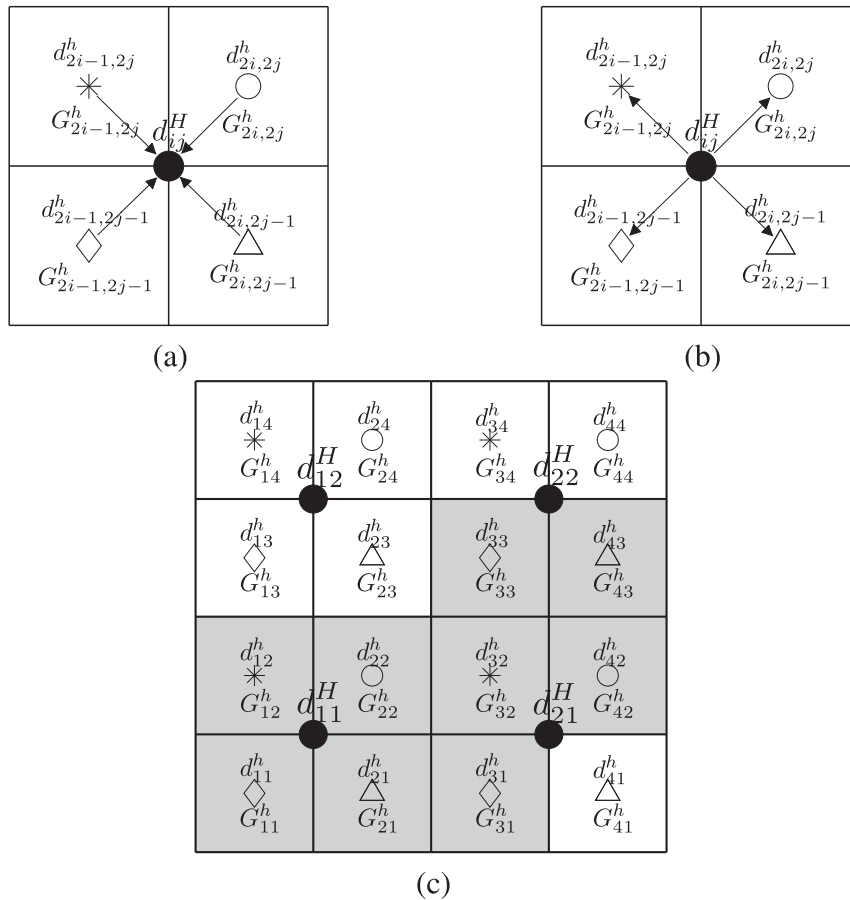
Fig. 7. (a) Restriction. (b) Interpolation. (c) $G^h = 1$ on gray region and $G^h = 0$ on white region.

wavy curved channel, sequential T-junctions, a sphere, and a wavy curved tube. Note that we will use either ϕ or c in our numerical experiments because two equations with different phase-field variables are equivalent.

3.1. The relation between the ϵ value and the width of the transition layer

In the first numerical experiment, we consider the relation between the ϵ value and the width of the transition layer for the CH equation. Across the interfacial region, the concentration field varies from 0.05 to 0.95 over a distance of approximately $4\sqrt{2}\tanh^{-1}(0.9)$ for c and varies from -0.9 to 0.9 over a distance of approximately $2\sqrt{2}\tanh^{-1}(0.9)$ for ϕ. Therefore, if we want this value to be approximately m grid points, the ϵ value needs to be taken as follows, respectively:

$$\epsilon_m = \frac{mh}{4\sqrt{2}\tanh^{-1}(0.9)} \quad \text{for } c \text{ and } \epsilon_m = \frac{mh}{2\sqrt{2}\tanh^{-1}(0.9)} \quad \text{for } \phi.$$

To confirm those formula, we run simulations with the initial data $\phi(x,y,0) = -0.4 + 0.001\,\mathrm{rand}\,(x,y)$ in a domain $\Omega = (0,64) \times (0,64)$ with a 64×64 mesh and $h = \Delta t = 1$. Here, the random number, rand (x,y), is uniformly distributed between -1 and 1. Shaded region indicates the embedded domain. Fig. 8(a) and (b) show contours from $\phi = -0.9$ to $\phi = 0.9$ increased by 0.2 with ϵ_3 and ϵ_{10} at $t = 5000$, respectively. From the two figures, we can see that the interfacial transition layer is about 3 and 10 grid points, respectively.

3.2. Convergence test

We should demonstrate the convergence of the proposed scheme. The initial state for the test is $\phi(x,y,0) = 0.8\cos(2\pi x)\cos(2\pi y)$ in a domain $\Omega_{in} = (-1,1) \times (-1,1) - (-0.5,0.5) \times (-0.5,0.5)$ (see Fig. 9). To calculate the accuracy of the proposed method, we perform a number of simulations on a set of increasingly finer grids. The numerical solutions are computed on the grids $h = 1/2^{n+1}$ for $n = 5, 6, 7, 8$, and 9. For each case, the calculation is run up to time $t = 0.01$ with the time step $\Delta t = 0.001/4^{n-5}$ and a fixed $\epsilon = 0.04$. We define the error of a grid to be the discrete l_2-norm of the difference between that grid and the average of the next finer grid cells covering it as follows. $e_{h/\frac{h}{2}ij} := \phi_{hij} - (\phi_{\frac{h}{2}2i,2j} + \phi_{\frac{h}{2}2i-1,2j} + \phi_{\frac{h}{2}2i,2j-1} + \phi_{\frac{h}{2}2i-1,2j-1})/4.$
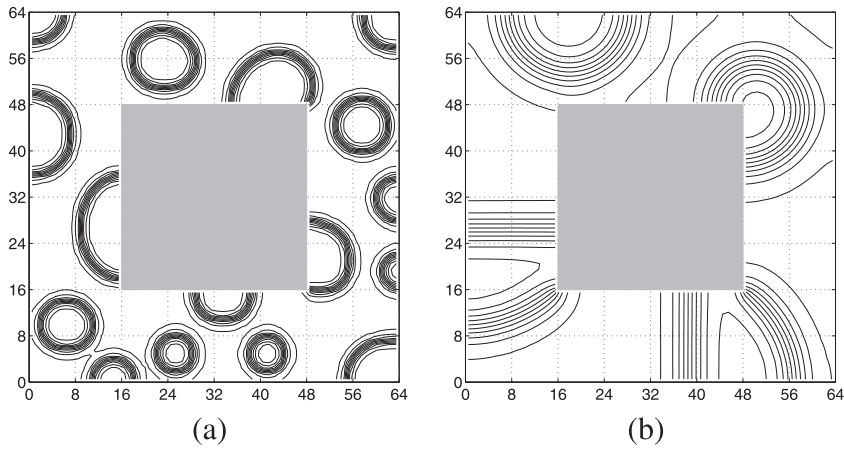
Fig. 8. The concentration contours at the nine levels from $\phi = -0.9$ to $\phi = 0.9$ increased by 0.2 with (a) ϵ_3 and (b) ϵ_{10}.
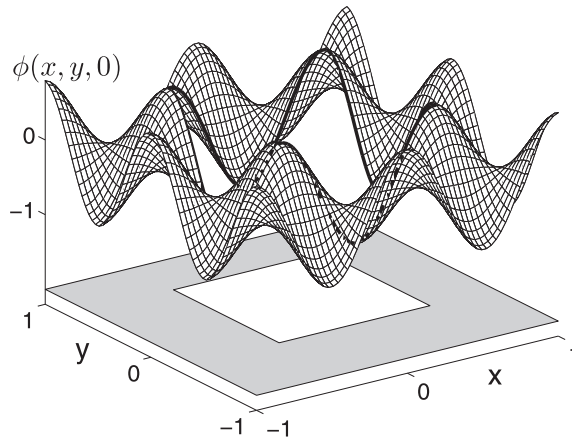

Fig. 9. The initial condition $\phi(x,y,0)$ with a small obstacle on $\Omega = (-1,1) \times (-1,1)$.

Table 1
The errors and rates of convergence for concentration ϕ.

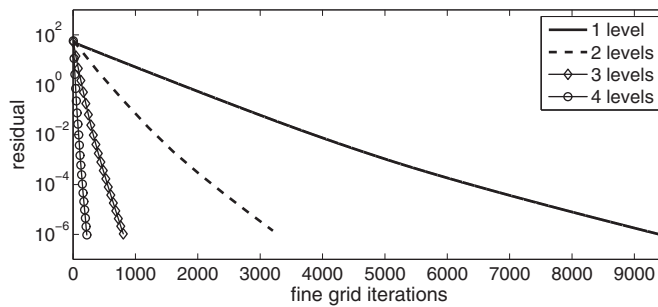| Case	32–64	Rate	64–128	Rate	128–256	Rate	256–512
l_2-error	1.44E−2	1.89	3.89 E−3	2.12	8.94E−4	2.05	2.16E−4

Fig. 10. The number of fine grid iterations needed to converge to a residual norm of 1.0E-6.

Table 2
The number of the fine grid iterations(FGI) for each level.

Level	1	2	3	4	5	6	7	8
FGI	9407	3289	809	221	65	29	29	29

Table 3
Stability constraint of Δt for the CN scheme and the proposed scheme.

Mesh size	Scheme	
	Crank–Nicolson scheme	Proposed scheme
$h = 1/64$	$\Delta t \leqslant 0.001120$	$\Delta t \leqslant 0.777$
$h = 1/128$	$\Delta t \leqslant 0.000270$	$\Delta t \leqslant 0.914$
$h = 1/256$	$\Delta t \leqslant 0.000672$	$\Delta t \leqslant 1.140$
$h = 1/512$	$\Delta t \leqslant 0.000166$	$\Delta t \leqslant 0.879$

And the rate of convergence is defined as the ratio of successive errors as $\log_2(\|e_{h/\frac{h}{2}}\|_2/\|e_{\frac{h}{2}/\frac{h}{4}}\|_2)$. Then Table 1 shows the errors and rates of convergence. The results suggest that the scheme is first-order accurate in time and second-order in space as we expect from the discretization.

3.3. Multigrid efficiency

To demonstrate the efficiency of the multigrid method, we perform the similar simulation as in [34]. The initial state and computational domain are same to the convergence test case. The parameters are ϵ_3, $h = 1/256$, $\Delta t = 1.0h$, and 512×512 mesh grid. All available vcycle levels are considered. Fig. 10 shows the maximum value of residual versus the number of fine grid iterations needed to converge to a residual norm of 1.0E-6 (we only plot four different levels for clarity). And in Table 2 the number of the fine grid iterations is listed for all levels. Significant improvement in the convergence is observed as we increase the vcycle level.

3.4. Stability comparison of two schemes

We compare the stability constraints for the CN scheme (6) and (7) and the proposed scheme (8) and (9). For each scheme, we calculate the maximum Δt so that stable solutions can be computed up to $T = 100\Delta t$. The initial concentration is taken to be $c(x,y,0) = 0.5 + 0.5\mathrm{rand}\,(x,y)$ in the computational domain $\Omega = (0,1) \times (0,1)$. Table 3 shows the results of the stability constraints of Δt with two schemes. We can see that the proposed scheme can use larger time steps. If the time step is reasonably small, then the stability of the proposed scheme seems independent of space step size.

3.5. The effect of constant and variable mobilities

3.5.1. Two-dimensional case
We examine the evolution of a random perturbation with the small magnitude about a mean composition and also consider numerical experiments highlighting the difference between the variable mobility $M(c) = c(1 - c)$ and the constant mobility $M(c) \equiv 0.25$ which is the maximum value of the variable mobility $M(c)$. The initial condition is taken to be $c(x,y,0) = 0.25 + 0.001\mathrm{rand}\,(x,y)$ in the computational domain $\Omega = (0,1) \times (0,1)$. And we take the simulation parameters: ϵ_4, $h = 1/128$, and $\Delta t = 0.5h$. We stop the numerical computations when the discrete l_2-norm of the difference between $(n + 1)$th and nth time step solutions becomes less than 10^{-6}, that is, $\|c^{n+1} - c^n\|_2 \leqslant 10^{-6}$. In the constant mobility case, we start the simulation with $c(x,y,7.813)$ from the variable mobility case.

In Fig. 11, the first row and the second row represent time evolutions of phase-fields with the constant and the variable mobilities, respectively. The final numerical solutions are stationary numerical solutions according to the stopping criteria. In the bottom row of figure, dark regions are nucleated. As the remaining regions grow, a numerical equilibrium state is reached. The variable mobility generally reduces the bulk diffusion, which corresponds to the interface-diffusion-controlled dynamics, i.e., diffusion process takes place along the interface between the two phases. This fact is made clear by comparing the results with the constant mobility. In the case of the constant mobility, the evolution leads to a single disk.

3.5.2. Three-dimensional case
Next, we investigate the effect of constant and variable mobilities on the three-dimensional domain. We simulate the evolution on a 64^3 mesh and use the following parameters: $\epsilon = 0.01$, $h = 1/64$, and $\Delta t = h$. The initial condition is taken to be $c(x,y,z,0) = 0.25 + 0.2\mathrm{rand}\,(x,y,z)$ in the computational domain $\Omega = (0,1) \times (0,1) \times (0,1)$. In the constant mobility case, we start the simulation with $c(x,y,z,62.5)$ from the variable mobility case. In Fig. 12, evolutions of the concentration $c(x,y,z,t)$
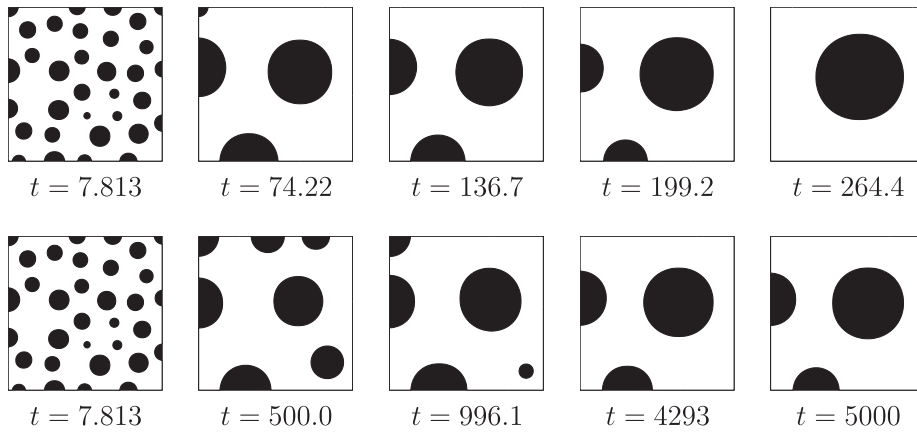
Fig. 11. Evolution of the concentration $c(x,y,t)$ with a constant mobility $M(c) \equiv 0.25$ (the top row) and a variable mobility $M(c) = c(1 - c)$ (the bottom row). The times are shown below each figure.
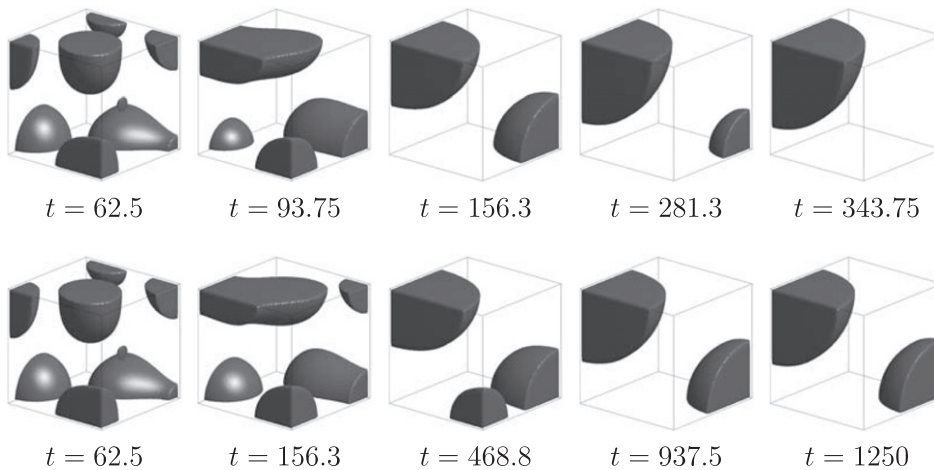

Fig. 12. Evolution of the concentration $c(x,y,z,t)$ with a constant mobility $M(c) \equiv 0.25$ (the top row) and a variable mobility $M(c) = c(1 - c)$ (the bottom row). The times are shown below each figure.

with a constant mobility $M(c) \equiv 0.25$ (the top row) and a variable mobility $M(c) = c(1 - c)$ (the bottom row) are shown. In the case of the variable mobility, two nucleated components are the numerical steady state solution. However, in the case of the constant mobility (the top row), only one component is shown.

3.6. The decrease of the total energy and the conservation of the average concentration

3.6.1. Rectangular domain case

In order to demonstrate that the numerical scheme inherits the energy decreasing property, we consider the evolution of the discrete total energy. We define a discrete energy functional by

$$\mathscr{E}^h(c^n) = (F(c^n), 1)_h + \frac{\epsilon^2}{2}|c^n|_1^2. \tag{25}$$

The initial state is taken to be $c(x,y,0) = 0.25 + 0.001\,\mathrm{rand}\,(x,y)$ in the computational domain $\Omega = (0,1) \times (0,1)$. Parameters $h = 1/128$, ϵ_4, and $\Delta t = 0.1$ are taken. In Fig. 13, the time evolution of the non-dimensional discrete total energy $\mathscr{E}^h(c^n)/\mathscr{E}^h(c^0)$ (solid line) is shown. We can see that the total discrete energy is non-increasing and the average concentration is preserved. And this numerical result agrees well with the total energy dissipation property. Also, the inscribed small figures are the concentration fields at the indicated times.
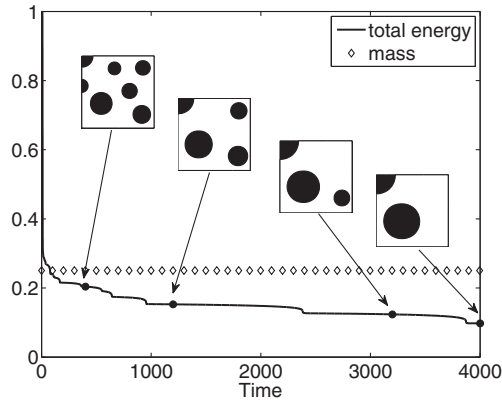
Fig. 13. The temporal evolution of non-dimensional discrete total energy $\mathscr{E}^h(c^n)/\mathscr{E}^h(c^0)$ (solid line) of the numerical solutions with the initial condition, $c(x,y,0) = 0.25 + 0.001$ rand (x,y).

3.6.2. Non-rectangular domain case

Now, we apply the numerical scheme for arbitrarily domains. The initial state is taken to be $\phi(x,y,0) = 0.25 + 0.001$ rand (x,y) in the computational domain $\Omega = (0,1) \times (0,1)$ with the mesh size 256×256 and the temporal step size $\Delta t = 0.1/256$. The interface Γ is a circle whose radius is 0.45 and center is located at $(0.5,0.5)$. Ω_{in} is the enclosed domain by the interface Γ. To demonstrate the discrete energy dissipation property in an arbitrary domain, we define a discrete energy functional by

$$\mathscr{E}^h(\phi^n) = (GF(\phi^n), 1)_h + \frac{\epsilon^2}{2}|G\phi^n|_1^2. \tag{26}$$

Fig. 14 shows that the discrete total energy is monotonically decreasing and the average concentration is conserved. The inscribed small figures are the evolution of the concentration field.

3.7. Evolution in complex domains

3.7.1. Spinodal decomposition in a wavy curved channel

We also apply our proposed scheme to a more complicated domain. First, we define the interface Γ which has the upper bound $u(x)$ and the lower bound $l(x)$ in the computational domain $\Omega = (0,4) \times (0,1)$. That is,

$$u(x) = 0.05\sqrt{x}\sin(3\pi x) + 0.75, \tag{27}$$
$$l(x) = 0.01x^2\cos(2\pi x) - 0.04\sin(6\pi x) + 0.3. \tag{28}$$

We simulate the evolution on a 1024×256 mesh size. The spatial size $h = 1/256$, the temporal size $\Delta t = 0.5h$, and ϵ_4 are used. The initial condition is taken to be $\phi(x,y,0) = -0.35 + 0.1$ rand (x,y). Fig. 15 shows the evolution of the concentration $\phi(x,y,t)$
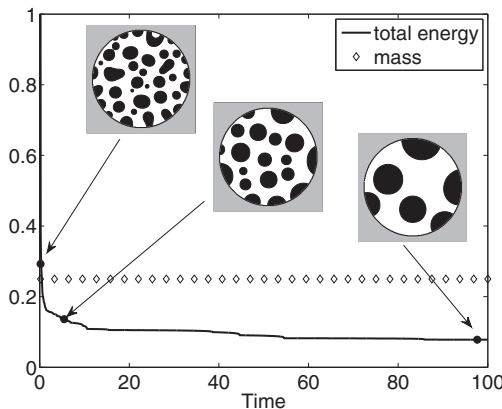

Fig. 14. The time dependent non-dimensional discrete total energy $\mathscr{E}^h(\phi^n)/\mathscr{E}^h(\phi^0)$ (solid line) of the numerical solutions with the initial condition, $\phi(x,y,0) = 0.25 + 0.001$ rand (x,y).
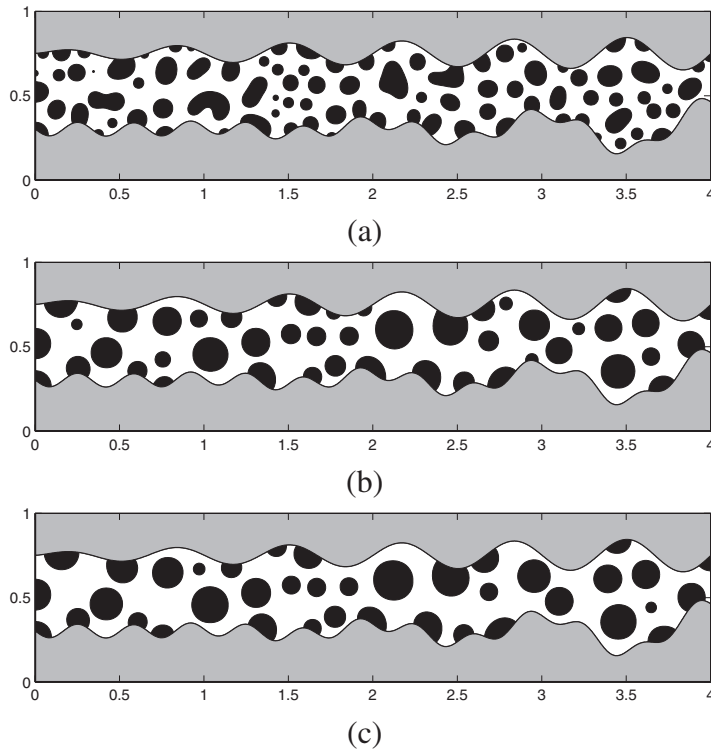
Fig. 15. Evolution of the concentration $\phi(x,y,t)$ with a variable mobility $M(\phi) = 1 - \phi^2$ in two-dimensional domain with the boundary control function G. The times of each figure are (a) t = 0.98, (b) t = 3.91, and (c) t = 9.77.
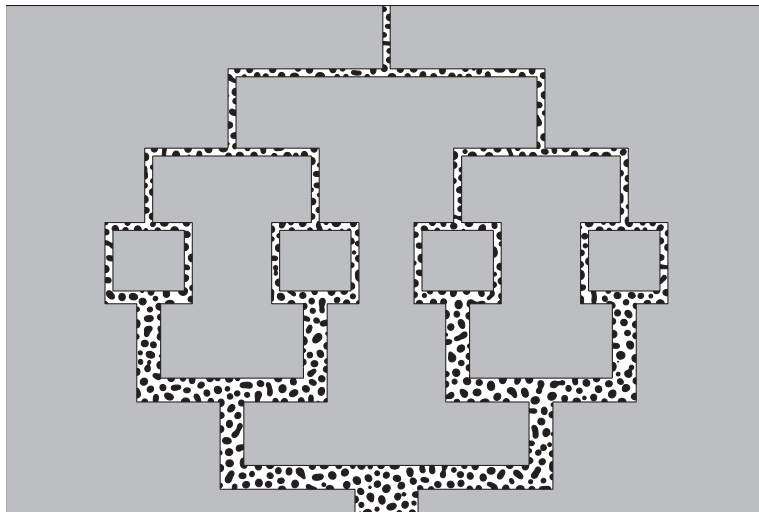

Fig. 16. Spinodal decomposition in sequential T-junctions.

with a variable mobility $M(\phi) = 1 - \phi^2$ and the boundary control function G. The times of each figure are (a) t = 0.98, (b) t = 3.91, and (c) t = 9.77.

3.7.2. Spinodal decomposition in sequential T-junctions

Microfluidic technology offers capabilities for the precise handling of small fluid volumes dispersed as droplets. Sequential application of the geometrically mediated T-junction is used to facilitate the precise conversion of large initial slugs of the dispersed phase into small droplets comparable in size to the channel [24]. We test our scheme on sequential T-junc-
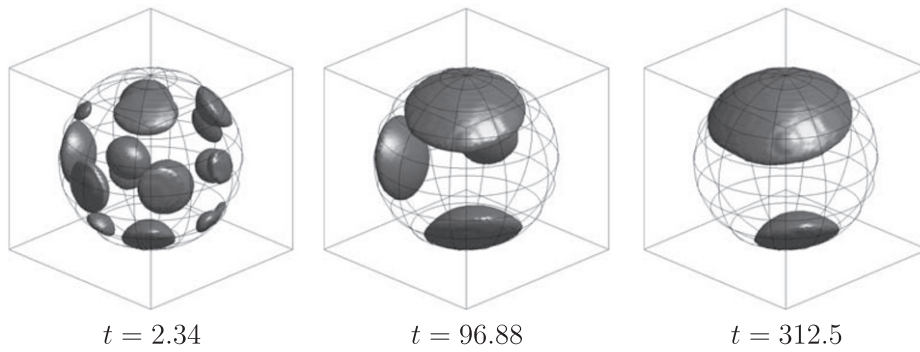
Fig. 17. Evolution of the concentration $c(x,y,z,t)$ with an initial condition $c(x,y,z,0) = 0.25 + 0.2$rand (x,y,z). The times are shown below each figure.

(a) Schematic   (b) $t = 3.13$

(c) $t = 71.88$ (d) $t = 156.25$
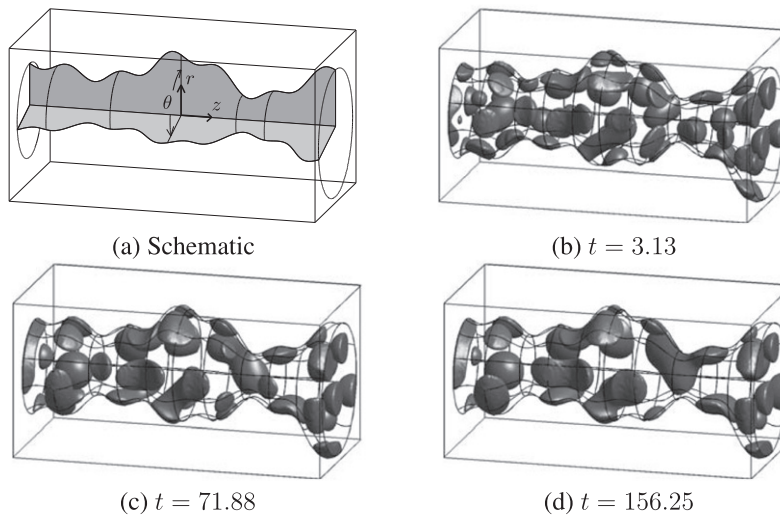
Fig. 18. Evolution of the concentration $c(x,y,z,t)$ with a variable mobility $M(c) = c(1 - c)$ in a three-dimensional domain. The times are shown below each figure.

tions. The numerical parameters are $h = 1/512$, $\Delta t = 0.1h$, and ϵ_4. The initial state is $\phi(x,y,0) = -0.4 + 0.001$rand (x,y) in the computational domain $\Omega = (0,3) \times (0,2)$. In Fig. 16, we see spinodal decomposition in sequential T-junctions at time $t = 0.0098$.

3.7.3. Spinodal decomposition in a sphere

We extend the numerical experiment to the three-dimensional space. The surface Γ is a sphere whose radius is 0.45 and center is (0.5, 0.5, 0.5). In this computation, we choose ϵ_4, $h = 1/64$, and $\Delta t = h$. The initial condition is taken to be $c(x,y,z,0) = 0.25 + 0.2$rand (x,y,z) on 64^3 mesh grid. In Fig. 17, Ω_{in} is inside mesh. For visibility, we plot only the longitude and latitude of the boundary of the domain Ω_{in}. This simulation also represents that the separation and small nucleation occur at an early stage ($t = 2.34$). After this initial phase separation, the coarsening process is developed slowly ($t = 96.88, 312.5$).

3.7.4. Spinodal decomposition in a wavy curved tube

Next, for a more complex domain simulation in 3D, we use the following surface:

$$r(\theta,z) = (0.01z^2 \cos(2\pi z) - 0.04 \sin(6\pi z) + 0.3)(0.9 - 0.3 \cos(\theta + \pi z)) \text{ for } 0 \leqslant \theta \leqslant 2\pi, \quad 2 \leqslant z \leqslant 4,$$

where r, θ, and z are distance from, azimuthal angle about, and distance along axis, respectively (see Fig. 18 (a)). The numerical parameters are $128 \times 128 \times 256$ mesh size, $h = 1/128$, $\Delta t = h$, and ϵ_3. The initial condition is $c(x,y,z,0) = 0.25 + 0.002$rand (x,y,z) in the computational domain $\Omega = (-0.5,0.5) \times (-0.5,0.5) \times (2,4)$. Fig. 18(b)–(d) show the evolution of the concentration $c(x,y,z,t)$ with a variable mobility $M(c) = 1 - c^2$. The times are shown below each figure.

4. Conclusions

We considered an efficient finite difference scheme for the Cahn–Hilliard equation with a variable mobility of a model for phase separation in a binary mixture. The numerical method is based on a type of the unconditionally gradient stable splitting discretization. We also extended the scheme to compute the Cahn–Hilliard equation in complex domains. And we proved the mass conservation property of the proposed discrete scheme for complex domains. The resulting discretized equations are solved by a multigrid method. Numerical simulations were presented to show the robustness and the superiority of the proposed scheme compared to other Crank–Nicolson scheme. The most salient feature is that although the algorithm is simple, it is applicable to many complex domains. Also, the algorithm is well suited to the multigrid method. The method described here is a specific application of a general formulism for constructing conservative finite difference methods for problems with complex embedded domains. Therefore, it is applicable to other partial differential equations in irregular domains.

Acknowledgments

References

[1] F.S. Bai, A. Spence, A.M. Stuart, Numerical computations of coarsening in the one-dimensional Cahn–Hilliard model of phase separation, Physica D 78 (1994) 155–165.
[2] J.W. Barrett, J.F. Blowey, Finite element approximation of the Cahn–Hilliard equation with concentration dependent mobility, Math. Comput. 68 (1999) 487–517.
[3] J.W. Barrett, J.F. Blowey, H. Garcke, Finite element approximation of the Cahn–Hilliard equation with degenerate mobility, SIAM J. Numer. Anal. 37 (1999) 286–318.
[4] J.W. Cahn, C.M. Elliott, A. Novick-Cohen, The Cahn–Hilliard equation with a concentration dependent mobility: Motion by minus the Laplacian of the mean curvature, Euro. J. Appl. Math. 7 (1996) 287–301.
[5] J.W. Cahn, J.E. Hilliard, Free energy of a non-uniform system. I. Interfacial free energy, J. Chem. Phys. 28 (1958) 258–267.
[6] J.W. Cahn, J.E. Hilliard, Spinodal decomposition: a reprise, Acta Metall. 19 (1971) 151–161.
[7] J.W. Cahn, J.E. Taylor, Surface motion by surface diffusion, Acta Metall. 42 (1994) 1045–1063.
[8] D. Calhoun, A cartesian grid method for solving the two-dimensional streamfunction-vorticity equations in irregular regions, J. Comput. Phys. 176 (2) (2002) 231–275.
[9] M. Copetti, C.M. Elliott, Kinetics of phase decomposition processes: numerical solutions to the Cahn–Hilliard equation, Mater. Sci. Technol. 6 (1990) 273–283.
[10] M.S. Day, P. Colella, M.J. Lijewski, C.A. Rendleman, D.L. Marcus, Embedded boundary algorithms for solving the Poisson equation on complex domains, Technical Report LBNL-41811, Lawrence Berkeley National Laboratory, May 1998.
[11] J.J. Eggleston, G.B. McFadden, P.W. Voorhees, A phase-field model for highly anisotropic interfacial energy, Physica D 150 (2001) 91–103.
[12] C.M. Elliott, D.A. French, Numerical studies of the Cahn–Hilliard equation for phase separation, IMA J. Appl. Math. 38 (1987) 97–128.
[13] D.J. Eyre, An unconditionally stable one-step scheme for gradient systems, Preprint (1997), <http://www.math.utah.edu/~eyre/research/methods/stable.ps>.
[14] D. Furihata, A stable and conservative finite difference scheme for the Cahn–Hilliard Equation, Numer. Math. 87 (2001) 675–699.
[15] D. Furihata, T. Matsuo, A stable, convergent, conservative and linear finite difference scheme for the Cahn–Hilliard equation, Jpn. J. Indust. Appl. Math. 20 (2003) 65–85.
[16] H. Gomez, V. Calo, Y. Bazilevs, T.J.R. Hughes, Isogeometric analysis of the Cahn–Hilliard phase field model, Comput. Methods Appl. Mech. Eng. 197 (2008) 4333–4352.
[17] Y. He, Y. Liu, T. Tang, On large time-stepping methods for the Cahn–Hilliard equation, Appl. Numer. Math. 57 (2007) 616–628.
[18] H. Johansen, P. Colella, A cartesian grid embedded boundary method for poissons equation on irregular domains, J. Comput. Phys. 147 1 (1998) 60–85.
[19] D. Kay, R. Welford, A multigrid finite element solver for the Cahn–Hilliard equation, J. Comput. Phys. 212 (2006) 288–304.
[20] J.S. Kim, A numerical method for the Cahn–Hilliard equation with a variable mobility, Commun. Nonlinear Sci. Numer. Simul. 12 (2007) 1560–1571.
[21] J.S. Kim, K. Kang, A numerical method for the ternary Cahn–Hilliard system with a degenerate mobility, Appl. Numer. Math. 59 (2009) 1029–1042.
[22] J.S. Kim, K. Kang, J.S. Lowengrub, Conservative multigrid methods for Cahn–Hilliard fluids, J. Comput. Phys. 193 (2004) 511–543.
[23] R.J. LeVeque, Z. Li, The immersed interface method for elliptic equations with discontinuous coefficients and singular sources, SIAM J. Numer. Anal. 31 (1994) 1019–1044.
[24] D.R. Link, S.L. Anna, D.A. Weitz, H.A. Stone, Geometrically mediated breakup of drops in microfluidic devices, Phys. Rev. Lett. 92 (2004) 054503.
[25] E.V.L. Mello, O.T.S. Filho, Numerical study of the Cahn–Hilliard equation in one, two and three dimensions, Physica A 347 (2005) 429–443.
[26] G. Sheng, T. Wang, Q. Du, K.G. Wang, Z.K. Liu, L.Q. Chen, Coarsening kinetics of a two phase mixture with highly disparate diffusion mobility, Comput. Phys. 8 (2010) 249–264.
[27] Z.Z. Sun, A second order accurate linearized difference scheme for the two-dimensional Cahn–Hilliard equation, Math. Comput. 64 (1995) 1463–1471.
[28] U. Trottenberg, C. Oosterlee, A. Schüller, Multigrid, Academic press, London, 2001.
[29] H.S. Udaykumar, R. Mittal, P. Rampunggoon, A. Khanna, A sharp interface Cartesian grid method for simulating flows with complex moving boundaries, J. Comput. Phys. 174 (2001) 345–380.
[30] G.N. Wells, E. Kuhl, K. Garikipati, A discontinuous Galerkin method for the Cahn–Hilliard equation, J. Comput. Phys. 218 (2006) 860–877.
[31] Y. Xia, Y. Xu, C.W. Shu, Local discontinuous Galerkin methods for the Cahn–Hilliard type equations, J. Comput. Phys. 227 (2007) 472–491.
[32] X. Ye, The Legendre collocation method for the Cahn–Hilliard equation, J. Comput. Appl. Math. 150 (2003) 87–108.
[33] J. Zhu, L.Q. Chen, J. Shen, V. Tikare, Coarsening kinetics from a variable mobility Cahn–Hilliard equation – application of semi-implicit Fourier spectral method, Phys. Rev. E 60 (1999) 3564–3572.
[34] M. Francois, W. Shyy, Computations of drop dynamics with the immersed boundary method, Numer. Heat Transf. B 44 (2003) 101–118.